Pneumatic Distortion Compensation for Aircraft Surface Pressure Sensing Devices

Stephen A. Whitmore*
NASA Ames Research Center, Dryden Flight Research Facility, Edwards, California 93523
and
Cornelius T. Leondes†
University of Washington, Seattle, Washington 98195

In this paper a technique of compensating for pneumatic distortion in aircraft surface pressure sensing devices is developed. The compensation allows conventional pressure sensing technology to obtain improved unsteady pressure measurements. Pressure distortion caused by frictional attenuation and pneumatic resonance within the sensing system makes obtaining unsteady pressure measurements by conventional sensors difficult. Typically, most of the distortion occurs within the pneumatic tubing used to transmit pressure impulses from the surface of the aircraft to the measurement transducer. This paper develops a second-order distortion model that accurately describes the behavior of the primary wave harmonic of the pneumatic tubing. The model is expressed in state-variable form and is coupled with standard results from minimum-variance estimation theory to develop an algorithm to compensate for the effects of pneumatic distortion. Both postflight and real-time algorithms are developed and evaluated using simulated and flight data. Covariance selection and filter-tuning examples are presented. Results presented verify that, given appropriate covariance magnitudes, the algorithms accurately reconstruct surface pressure values from remotely sensed pressure measurements.

Nomenclature

A_c	= cross-sectional area of pneumatic tubing
B	= state equation input geometry matrix
C	= observation matrix
c	= sonic velocity
D	= pressure tubing cross-sectional diameter
G	= a priori variance of the pressure measurement noise
G_{k+1}	= a priori measurement noise covariance matrix
g_{k+1}	= measurement noise function
I	= identity matrix
K	= Kalman filter gain matrix
L	= length of pneumatic tubing
N	= number of data frames available
P	= filter error covariance matrix
P_a	= initial local pressure
P_L	= downstream pressure output
P_0	= prescribed input pressure function
$P(x,t)$	= pressure function
Q	= state noise covariance matrix
Q_u	= a priori variance of input pressure residual
R	= acoustic resistance of pneumatic configuration
$\tilde{R}$	= deconvolution output residual vector
s	= Laplace operator
t	= time coordinate
U	= actual input vector
$\hat{U}$	= input vector estimate
V	= enclosed transducer volume
V_e	= effective sensor volume, $V + [A_cL]/2$
X	= state vector
$\hat{X}$	= state vector estimate
x	= spatial coordinate
Z	= output vector
$\hat{Z}$	= output vector estimate
$\tilde{Z}$	= predicted output residual vector
Γ	= prescribed input vector
Δ	= recursive residual error matrix
Δt	= discretization time interval
δ	= input error vector
$\hat{\delta}$	= input error vector estimate
μ	= dynamic viscosity
ξ	= damping ratio of second-order model
ρ_0	= initial density
Φ	= state equation transition matrix
ω_n	= natural frequency of second-order model

Data Frame Indices

$k-1$	= data frame index, time $(k-1)\Delta t$
k	= data frame index, time $(k)\Delta t$
$k+1$	= data frame index, time $(k+1)\Delta t$
$k/(k-1)$	= filter value at frame k based on $k-1$ observations
$(k+1)/k$	= filter value at frame $k+1$ based on k observations
$(k+1)/(k+1)$	= filter value at frame $k+1$ based on $k+1$ observations
k/N	= smoother value at frame k based on N observations
$(k+1)/N$	= smoother value at frame $k+1$ based on N observations
$(N+1)/N$	= smoother value at frame $N+1$ based on N observations

Received Feb. 10, 1990; revision received Oct. 12, 1990; accepted for publication Dec. 9, 1990.

*Aerospace Engineer, P.O. Box 273. Member AIAA.
†Professor, Electrical Engineering Department, FT-10. Member AIAA.

Introduction

RECENT advances in aircraft performance and maneuver capability have complicated the problem of flight control augmentation. Increasingly, aircraft system designs use aerodynamic parameters derived from pneumatic measurements as

control system feedbacks. To be feedback quality, these data must be measured with accuracy and dynamic fidelity. Since typically aerodynamic data are pneumatically sensed, this is a difficult task for conventional technology pressure sensors. The primary difficulty in obtaining high-fidelity unsteady pressure measurements using conventional sensors is acoustical distortion due to frictional attenuation and pneumatic resonance within the pressure sensing system. New nonacoustic pressure sensing technologies such as piezo-film or laser-based optical techniques need to be developed. Unfortunately, for flight applications, these technologies are still undeveloped and will not be reliably proven for at least a decade. Additionally, these advanced technologies are expensive. In light of these limitations, a research effort was initiated at NASA Ames/Dryden, and supported by the University of California, Los Angeles (UCLA), to develop a technique for measuring unsteady pressure data using conventional pressure sensing technology. Preliminary results of this research have already been published in Refs. 1–4.

Typically, most of the distortion occurs within the pneumatic tubing used to transmit pressure impulses from the surface of the aircraft to the measurement transducer. To avoid pneumatic distortion, experiment designers mount the pressure sensor at the surface of the aircraft, a process called in situ mounting. In some cases, this technique is a viable solution. In most cases, as when many pressures must be measured in a small surface area or when pressure is sensed in a hostile environment, pneumatic tubing is required to transmit pressure from the surface of the aircraft to the transducer. For most flight test applications, pressure transduction devices are located somewhere within the internal cavity of the aircraft.

Pressure variations at the surface propagate as waves from the upstream end of the pneumatic tubing to the pressure transducer. The wave propagation is damped by frictional attenuation along the walls of the pneumatic tubing. This damping causes spectral attenuation of the pressure output, and produces both a magnitude attenuation and a phase lag. As the wave reaches the downstream (transducer) end of the pneumatic tubing, it is reflected back up the tube. Depending upon the frequency of incoming waves and the length of the pneumatic tubing, the reflected waves either cancel or reinforce incoming pressure waves. If the waves cancel, further spectral attenuation occurs; if the waves reinforce, the power of the incoming wave is amplified and resonance occurs. Spectral distortion will not occur in zero volume configurations (with in situ mounting) only.

A considerable body of information concerning the effects of pneumatic distortion on pressure sensors is available. Early analyses modeled pneumatic tubing dynamics assuming either highly damped[5] or lightly damped[6] measurement configurations. Later work accounted for sensors with arbitrary damping, but required either step[7] or sinusoidal[8] inputs to be prescribed. A wave model, solvable numerically for arbitrary inputs and applicable to sensors of arbitrary damping, was developed in Refs. 1 and 3. The model, based upon the unsteady equations of momentum and continuity, was extensively verified by comparisons to special-case analytical solutions, and laboratory and flight data. A postflight compensation technique developed using the wave model, which relies on Fourier transform analyses and spectral deconvolution, was reported in Ref. 4. Because the technique uses transform analyses, it inherently cannot be applied in real time. Further, the technique does not control noise amplification during the deconvolution, and resulting input estimates are often overly noisy.

This paper summarizes results presented in Refs. 1–3, and extends the work of Ref. 4. Here, the full-wave model is reduced to a second-order model describing the behavior of the primary tubing harmonic. The second-order model, more amenable to analysis, is used in conjunction with minimum-variance deconvolution techniques to develop both postflight and real-time compensation methods that control noise over-

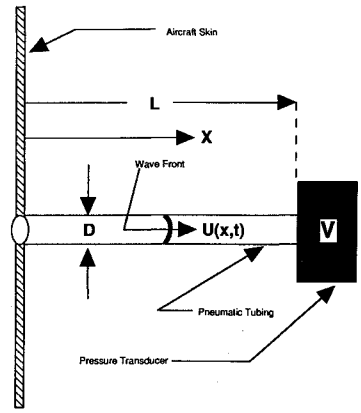

Fig. 1 Schematic of pressure sensing device.

amplification during the deconvolution process. This paper discusses modeling and compensating for the internal acoustics of the pressure sensor only; external effects, such as orifice disturbance of the flow, will not be modeled. For the remainder of the paper, the term *transducer* is used to describe the actual physical transduction device and its associated electronics. The term *sensor* is used to describe the transducer, surface pressure port, and all associated pneumatic tubing and pressure fittings.

Modeling and Analysis

This section presents the idealized configuration to be analyzed first. Next, the full-wave model of Refs. 1 and 3 is reduced to a simple second-order filter that retains most of the dynamic characteristics of the complete model. The second-order model is written in state variable form, and frequency-response comparisons with the full-wave model are presented.

Idealized Pressure Sensor Geometry and Conditions

The pressure sensor configuration, Fig. 1, is modeled as a straight cylindrical tube with constant diameter D and length L. A small volume V, representing the internal volume of the pressure transducer, is attached to the downstream end. A longitudinal coordinate x is defined starting at the upstream end of the tube, and a time coordinate t is defined relative to an arbitrary starting time.

A small pressure pulse is introduced at the upstream end of the pneumatic tubing and propagates down the tube as a longitudinal wave. The flow velocity is assumed to be approximately the radial average and, as a result, pressure variations within the sensor are modeled as a function of x and t only. Since the sensor is closed at one end and the input amplitude is small, flow velocities remain small and air density within the sensor is assumed to experience only small variations. Similarly, since the flow velocities are small, in the absence of extensive external heat transfer, temperatures within the sensor remain nearly constant.

Governing Equations

The governing equations of the full-wave model are derived in Ref. 3. This model, a hyperbolic boundary value problem (BVP), prescribes the input pressure and solves for the downstream output. The basic dynamics equations are

$$\frac{\partial^2 p(x,t)}{\partial t^2} + \frac{R}{\rho_0}\frac{\partial p(x,t)}{\partial t} = c^2 \frac{\partial^2 p(x,t)}{\partial x^2} \tag{1a}$$

Subject to the boundary conditions

$$\frac{\mathrm{d}^2 p(L,t)}{\mathrm{d}t^2} + \frac{R}{\rho_0}\frac{\mathrm{d}p(L,t)}{\mathrm{d}t} + \frac{A_c c^2}{V}\left\{\frac{\partial p(x,t)}{\partial x}\right\}_{x=L} = 0 \tag{1b}$$

$$p(0,t) = P_0(t) \tag{1c}$$

and the initial condition

$$p(x,0) = P_a \tag{1d}$$

In Eqs. (1a) and (1b), R is the acoustical resistance of the system, and for laminar flow

$$R = 8\pi\mu/A_c$$

where μ is the dynamic viscosity of air. By evaluating the acoustical resistance based on the Blasius friction law,[9] the BVP is easily extended to describe turbulent flow. This extension is derived in detail in Ref. 3.

Reducing the Wave Model to a Second-Order Equation

Although the BVP cannot be generally solved in closed form in the time domain, the model can be solved in closed form in the frequency domain.[4] Numerical techniques for solving the BVP in the time domain for arbitrary inputs are developed in Refs. 1 and 3. In the frequency domain, the closed form solution is

$$\frac{P_L(s)}{P_0(s)} = \frac{1}{\cosh[\sqrt{s^2 + (R/\rho_0)s}\,L/c] + [V\sqrt{s^2 + (R/\rho_0)s}/A_c c]\sinh[\sqrt{s^2 + (R/\rho_0)s}\,L/c]} \tag{2a}$$

When Eq. (2a) is inverse Laplace transformed, the BVP reduces to a single ordinary differential equation (ODE) with an infinite number of harmonic terms. The resulting ODE is

$$\left\{1 + \sum_{m=1}^{\infty}\left(\frac{d^2}{dt^2} + \frac{R}{\rho_0}\frac{d}{dt}\right)^m\left[\left(\frac{[L/c]^{2m}}{(2m)!}\right) + \frac{V}{A_c c}\left(\frac{[L/c]^{2m-1}}{(2m-1)!}\right)\right]\right\}P_L(t) = P_0(t) \tag{2b}$$

where $P_L(t) = P(L,t)$, $P_0(t) = P(0,t)$, and each m represents a resonant harmonic of the pneumatic tubing. If Eq. (2b) is truncated after the first harmonic, then a second-order model of the the primary harmonic results

$$\frac{d^2P_L(t)}{dt^2} + 2\xi\omega_n\frac{dP_L(t)}{dt} + \omega_n^2 P_L(t) = \omega_n^2 P_0(t) \tag{2c}$$

where the natural frequency is given by

$$\omega_n^2 = \frac{c^2 A_c}{LV_e}$$

with

$$V_e = V + \frac{LA_c}{2}$$

and the damping ratio is given by

$$\xi = \frac{R}{2\omega_n\rho_0}$$

Equation (2c) is easily converted to state variable form and integrated using implicit Euler integration[10] to give a discrete time state variable model of the form

$$X_{k+1} = \Phi X_k + BU_{k+1} \tag{2d}$$

where

$$X_{k+1} = \begin{bmatrix} P_{L_k} \\ P_{L_{k+1}} \end{bmatrix}, \quad X_k = \begin{bmatrix} P_{L_{k-1}} \\ P_{L_k} \end{bmatrix}, \quad U_{k+1} = [P_{0_{k+1}}]$$

$$\Phi = \begin{bmatrix} 0 & 1 \\ \dfrac{-1}{1 + 2\xi\omega_n\Delta t + (\omega_n\Delta t)^2} & \dfrac{2(1 + \xi\omega_n\Delta t)}{1 + 2\xi\omega_n\Delta t + (\omega_n\Delta t)^2} \end{bmatrix}$$

$$B = \begin{bmatrix} 0 \\ \dfrac{(\omega_n\Delta t)^2}{1 + 2\xi\omega_n\Delta t + (\omega_n\Delta t)^2} \end{bmatrix}$$

As mentioned previously, Eq. (2d) retains most of the frequency and time-response characteristics of the original wave model up through the first wave harmonic. Figure 2 displays sample frequency response comparisons for an overdamped sensor with pneumatic tubing 8 ft long and 0.06 in. in diameter. For this case, the transducer volume is considered to be negligible. At an altitude of 40,000 ft, the damping ratio of the second-order model is 1.93, and the natural frequency is 26.75 Hz. Figure 3 presents similar frequency response comparisons for a lightly damped configuration with a 2-ft-long, 0.06-in.-diam pneumatic tubing and negligible transducer volume. At an altitude of 20,000 ft, the damping ratio of the second-order model is 0.25 and the natural frequency is 108.93 Hz.

For both figures, the comparisons are good up to the natural frequency of the second-order model. Beyond the natural frequency, both the magnitude and phase angle comparisons diverge. The reason for the divergence is clear; the second-order approximation does not allow for higher-order wave harmonics, whereas the wave model does. Thus, at frequencies significantly beyond the first harmonic, a second-order model may not be acceptable, and more harmonics of Eq. (2b) should be retained. For each harmonic that is retained, an additional two states are added to the state-variable equation.

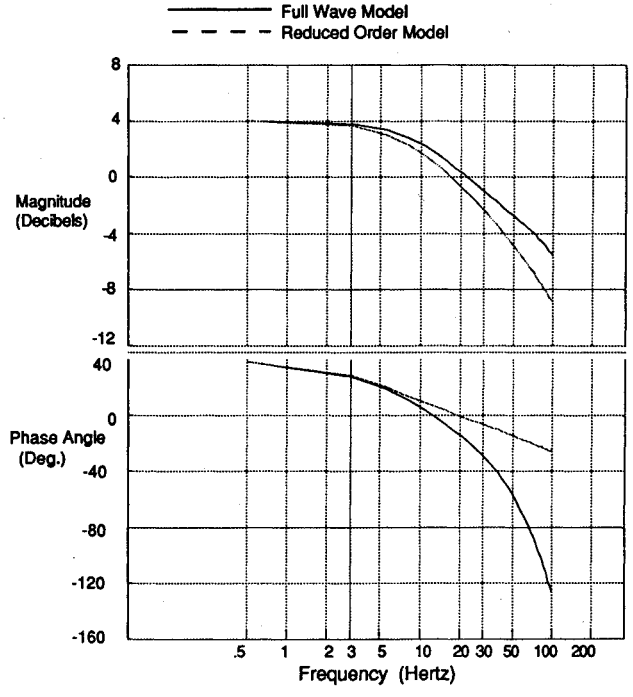

Fig. 2 Frequency response comparisons: full- and reduced-order models for overdamped sensor configuration.

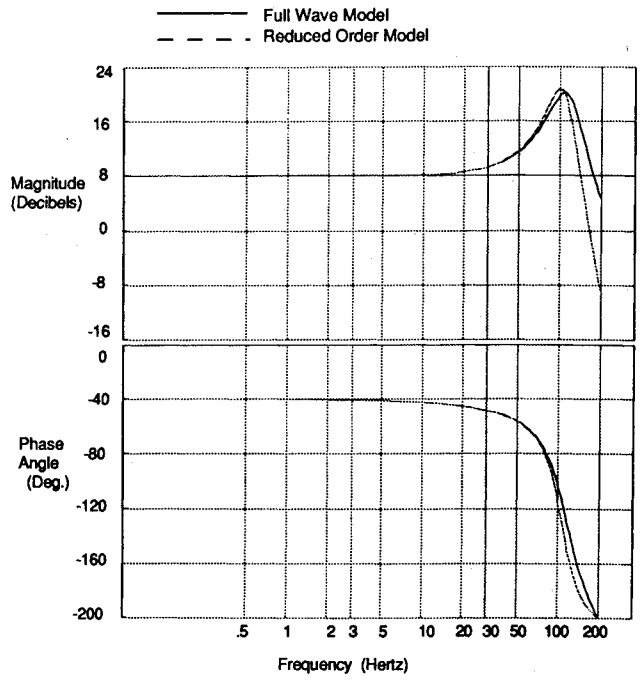

Fig. 3 Frequency response comparisons: full- and reduced-order models for underdamped sensor configuration.

For the purpose of this analysis, the additional complexity introduced by adding additional wave harmonics to the second-order model is considered to be unjustified.

Deriving the Compensation Algorithm

If Eq. (2d) is solved for $P_{0_{k+1}}$ in terms of $P_{L_{k+1}}$, the resulting equation is numerically ill-conditioned and, if used as a compensation algorithm, small changes in P_L will produce large changes in P_0. For real pressure data, measurement noise would be overamplified by the numerical instability and overwhelm the input pressure estimate. For a practical compensation algorithm, measurement noise must be identified and controlled as part of the estimation loop. Compensation algorithms performing the error control function are presented in this section. The algorithms are used to infer the external input to the system, based on the measured output at the transducer. In general, the technique of inferring the input, given the system structure and a measurement of the output, is known as deconvolution.

First, a general deconvolution algorithm, as developed in Ref. 3, is presented. The technique, developed using the techniques of minimum-variance estimation theory, is a derivative of results presented in Refs. 11–13. Both postflight and real-time algorithm versions are presented. Once the general algorithms have been presented, they are applied to the pressure compensation problem.

Minimum-Variance Deconvolution

The basic approach of the deconvolution algorithm is to prescribe an input to the state variable model and then identify the residual between the prescribed input and the actual input, using minimum-variance estimation techniques. Defining

$$U_{k+1} = \Gamma_{k+1} + \delta_{k+1} \tag{3a}$$

Eq. (2d) becomes

$$X_{k+1} = \Phi X_K + B\Gamma_{k+1} + B\delta_{k+1} \tag{3b}$$

where U_{k+1} is the actual input to the system, Γ_{k+1} is the prescribed (nonrandom) input to the system model, and δ_{k+1} is a random process modeling the residual between the actual and prescribed inputs. The covariance of δ_{k+1} is given a priori as

$$\text{cov}[\delta_{k+1}] = Q_{k+1}$$

Measurements Z_{k+1} of the state vector are observed in the presence of noise

$$Z_{k+1} = CX_K + g_{k+1} \tag{3c}$$

and the covariance of g_{k+1} is given a priori as

$$\text{cov}[g_{k+1}] = G_{k+1}$$

For the remainder of this discussion, all minimum-variance algorithm notation will follow the conventions of Ref. 14. For notational convenience, the state transition matrix Φ and the input and measurement geometry matrices B and C are written as constants. The algorithms as presented do not restrict these values to be constants.

Two complete estimation algorithms are presented. The first algorithm, intended for postflight data reconstruction, is implemented as a two-pass forward filter/backward smoother. As developed in Ref. 3, the postflight smoothing algorithm uses all available data measurements—both past and future. The algorithm, a hybrid of the Kalman filter and the Rauch smoother,[14] uses nonwhite information deposited in the Kalman filter predicted output residuals to identify differences between the prescribed input and the "true" input during the reverse pass of the algorithm. The second algorithm, intended for real time operation, is derived from the smoothing algorithm and implemented as a time-recursive filter. This algorithm does not take advantage of future observations of the system output, but instead relies on only current and past observations to predict the future input.

Post-Flight Smoothing Algorithm

Assuming that observations of the system output are available for data frames $k = 0, 1, \ldots, N$, the forward-pass Kalman filter loop is performed for every data frame

$$\hat{X}_{(k+1)/k} = \Phi\hat{X}_{k/k} + B\Gamma_{k+1} \tag{4a}$$

$$\hat{P}_{(k+1)/k} = \Phi\hat{P}_{k/k}\Phi^T + BQ_{k+1}B^T \tag{4b}$$

$$\tilde{Z}_{(k+1)/k} = Z_{k+1} - C\hat{X}_{(k+1)/k} \tag{4c}$$

$$K_{k+1} = P_{(k+1)/k}C^T(CP_{(k+1)/k}C^T + G_{k+1})^{-1} \tag{4d}$$

$$\hat{X}_{(k+1)/(k+1)} = \hat{X}_{(k+1)/k} + K_{k+1}\tilde{Z}_{(k+1)/k} \tag{4e}$$

$$\hat{P}_{(k+1)/(k+1)} = [I - K_{k+1}C]\hat{P}_{(k+1)/k} \tag{4f}$$

where $P_{(k+1)/k}$ is the predicted filter error covariance, $P_{(k+1)/(k+1)}$ is the adjusted filter error covariance based upon the current observation, K_{k+1} is the Kalman filter gain matrix, and $\tilde{Z}_{(k+1)/k}$ is the predicted output residual. The matrices $BQ_{k+1}B^T$ and G_{k+1} are the a priori covariances of the input and measurement noise processes. The vectors $\hat{X}_{(k+1)/k}$ and $\hat{X}_{(k+1)/(k+1)}$ are the predicted and corrected estimates of the filter state vector. Resulting estimates for the state vector, the error covariances, and the predicted output residuals, must be stored at the end of each forward-pass data frame.

At this point the input residual estimation loop is performed backward from the final data frame for $k = N, N-1, \ldots, 1, 0$, using stored data. Defining the deconvolution output residual vector

$$\tilde{R}_{k/N} = (P_{k/(k-1)})^{-1}[\hat{X}_{k/N} - \hat{X}_{k/(k-1)}] \tag{5a}$$

which relates to the input error vector estimate by

$$\hat{\delta}_{k/N} = Q_k B^T \tilde{R}_{k/N} \tag{5b}$$

As derived in Ref. 3, the backward recursion for the deconvolution output residual vector is

$$\tilde{R}_{k/N} = \Delta_k^T \tilde{R}_{(k+1)/N} + C^T(CP_{(k+1)/k}C^T + G_{k+1})^{-1}\tilde{Z}_{(k+1)/k} \quad (5c)$$

where

$$\Delta_k^T = (\Phi[I - K_k C])^T$$

The minimum-variance input estimate is extracted from the prescribed input by

$$\hat{U}_{k/N} = \Gamma_{k/N} + \hat{\delta}_{k/N}$$

At the start of the backward recursion, the final value for the residual vector $\tilde{R}_{(N+1)/N}$ is evaluated from Eq. (5a), with index k replaced by N

$$\tilde{R}_{(N+1)/N} = [P_{(N+1)/N}]^{-1}[\hat{X}_{(N+1)/N} - \hat{X}_{(N+1)/N}] = 0 \quad (5d)$$

Real-Time Filtering Algorithm

The real-time algorithm relies only on past and current data to perform the estimation. If measurements are available for data frames 0, 1, . . . , $k + 1$, the residual estimation is performed by replacing indices k and N in Eq. (5b) by $k + 1$

$$\hat{\delta}_{(k+1)/(k+1)} = Q_{k+1}B^T\tilde{R}_{(k+1)/(k+1)} \quad (6a)$$

But

$$\tilde{R}_{(k+1)/(k+1)} = [P_{(k+1)/(k+1)}]^{-1}[\hat{X}_{(k+1)/(k+1)} - \hat{X}_{(k+1)/k}] \quad (6b)$$

and, if Eq. (6b) is substituted into Eq. (6a) along with Eqs. (4e) (Kalman filter state update) and (4d) (Kalman filter gain), and the results are rearranged,

$$\hat{\delta}_{(k+1)/(k+1)} = Q_{k+1}B^TC^T(CP_{(k+1)/k}C^T + G_{k+1})^{-1}\tilde{Z}_{(k+1)/k} \quad (6c)$$

Finally, the input estimate is extracted from the prescribed input by

$$\hat{U}_{(k+1)/(k+1)} = \Gamma_{(k+1)/(k+1)} + \hat{\delta}_{(k+1)/(k+1)} \quad (6d)$$

If Eqs. (6c) and (6d) are appended to the Kalman filter equations (4a)–(4f), the real-time deconvolution algorithm results.

Results and Discussion

The minimum variance deconvolution algorithms are now applied to pneumatic distortion. For this analysis, the prescribed input function Γ_{k+1} is evaluated by solving Eq. (2d) for the input pressure in terms of the output pressure, and evaluating the result using state estimates from previous filter time recursions and currently measured pressure data. Pressure measurement noise is estimated and controlled by the deconvolution algorithm through judicious selection of the a priori state and measurement noise covariance matrices. Illustrations of the covariance selection process, known as *filter tuning*, are presented first. The illustrations are performed using simulated data. Next the deconvolution algorithms are applied to flight data. Analyses are performed using both the postflight and real-time algorithms. Comparisons with reference pressure data obtained from flight experiments are presented.

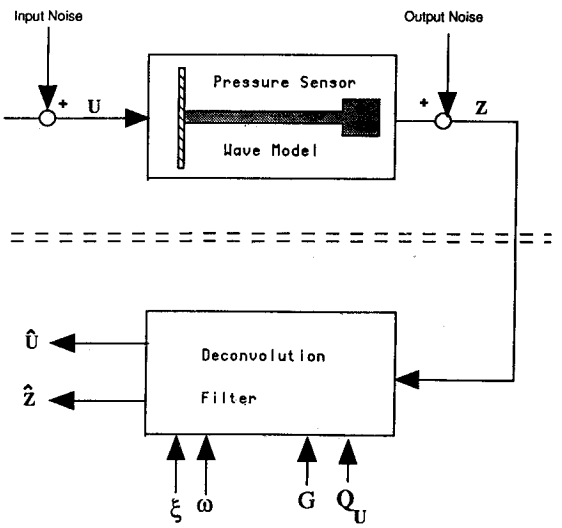

Fig. 4 Schematic of deconvolution simulation scheme.

Filter Tuning

To illustrate the tuning process, simulated data is used, because the actual measurement and input error covariances can be predefined. As derived in the previous section, the covariances may be time varying; however, for this analysis all error processes are assumed to be stationary, and thus all covariances are constant. Derived from Eq. (2d), for the pressure compensation problem, the state noise covariance matrix is given by

$$BQ_{k+1}B^T = \begin{bmatrix} 0 & 0 \\ 0 & Q_U\left\{\dfrac{(\omega_n\Delta t)^2}{1 + 2\xi\omega_n\Delta t + (\omega_n\Delta t)^2}\right\}^2 \end{bmatrix}$$

for all k, where Q_U is the a priori variance of prescribed input pressure residual. Similarly, assuming that the measurement noise process is white and stationary, the measurement noise covariance is given by the diagonal matrix

$$G_{k+1} = \begin{bmatrix} G & 0 \\ 0 & G \end{bmatrix}$$

for all k, where G is the a priori variance of the pressure measurement noise.

First, the minimum variance deconvolution analysis is performed using the postflight smoothing algorithm. The process is illustrated in Fig. 4. Simulated data are generated using numerical solutions of the full-wave model, assuming the overdamped configuration associated with Fig. 2. A prescribed input is superimposed with additive zero-mean white noise, with a variance (Q_u) of 1.0 lbf/ft^2. The result (U) is input to the wave model. Simulated zero-mean white noise with a variance (G) of 0.1 lbf/ft^2 is superimposed on the wave model output to give a pseudomeasurement time history (Z), which is used to perform the deconvolution. The resulting deconvolution estimates of the input and output are indicated by the symbols $\hat{U}$ and $\hat{Z}$. Values of Q_u and G are selected open-loop and are uncorrelated.

Figures 5 and 6 demonstrate the effects that selected values of G have on the estimates of U. In these figures the value of Q_U is fixed at the actual value of 1.0 lbf/ft^2, whereas the value for G is varied. Recall that the actual measurement error variance of G is 0.1 lbf/ft^2.

Figure 5 depicts the deconvolution results for $G = 10.0$ lbf/ft^2, a value that is much too large. Three time history graphs are presented. Depicted in the lower graph are time history overplots of the "measured" downstream pressure output Z (solid line), and the deconvolution estimate of the input pressure $\hat{U}$ (dashed line). Depicted in the middle graph are time history overplots of the measured output Z (solid line), and the estimated output $\hat{Z}$ (dashed line). Depicted in the upper graph are time history overplots of the actual input $\hat{U}$ (solid line), and the estimated input $\hat{U}$ (dashed line). Comparisons are poor. Clearly this set of weights does not allow the estimation algorithm to extract enough information from the measured pressure data; the resulting estimates are overly smoothed and tend to drift around the actual values.

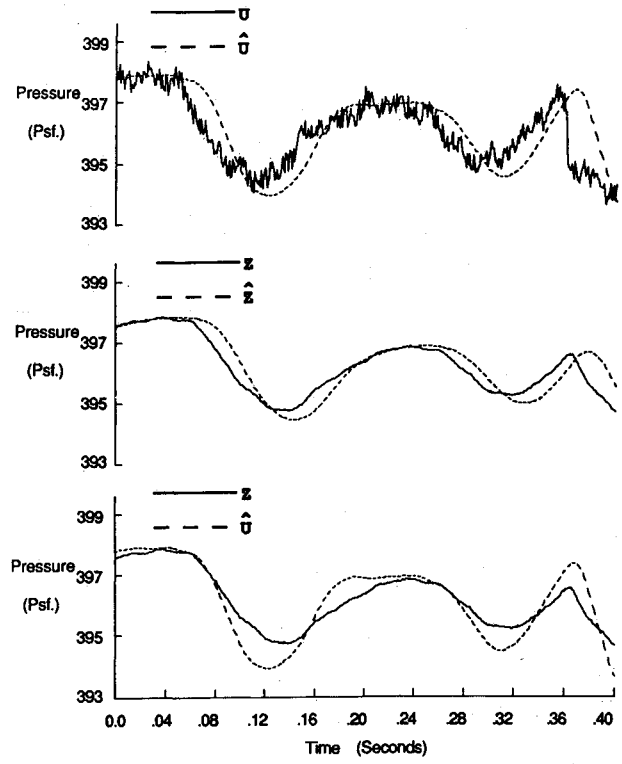

Fig. 5 Filter tuning example: effect of improperly selected measurement error covariance, $Q_u = 1.0$, $G = 10.0$.

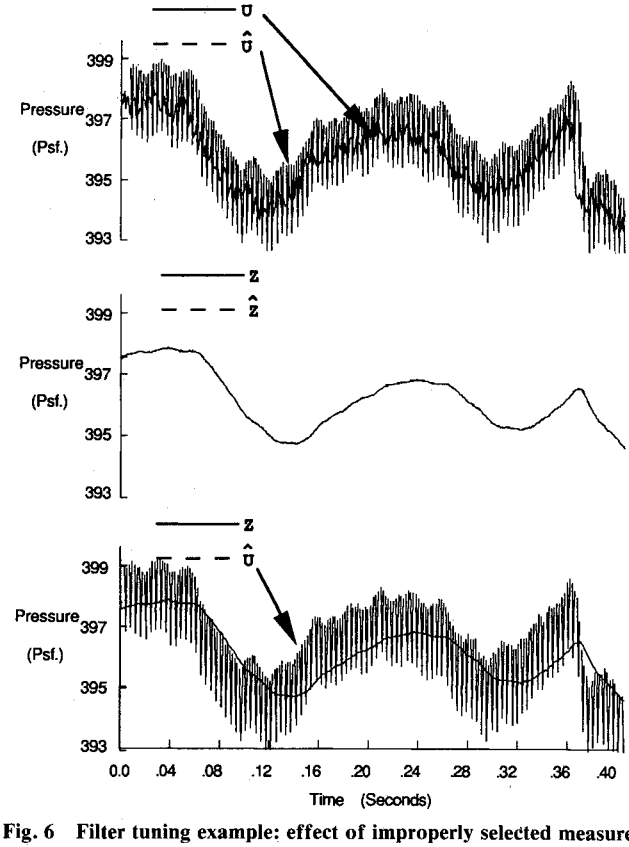

Fig. 6 Filter tuning example: effect of improperly selected measurement error covariance, $Q_u = 1.0$, $G = 0.01$.

The above situation cannot be improved by arbitrarily lowering the value for G. This point is illustrated in Fig. 6. Depicted are similar time history comparisons; however, in this instance, the value for G is set at 0.01 lbf/ft^2, a value that is far too small. The result is a virtually perfect match between the measured and predicted output, and a grossly corrupted

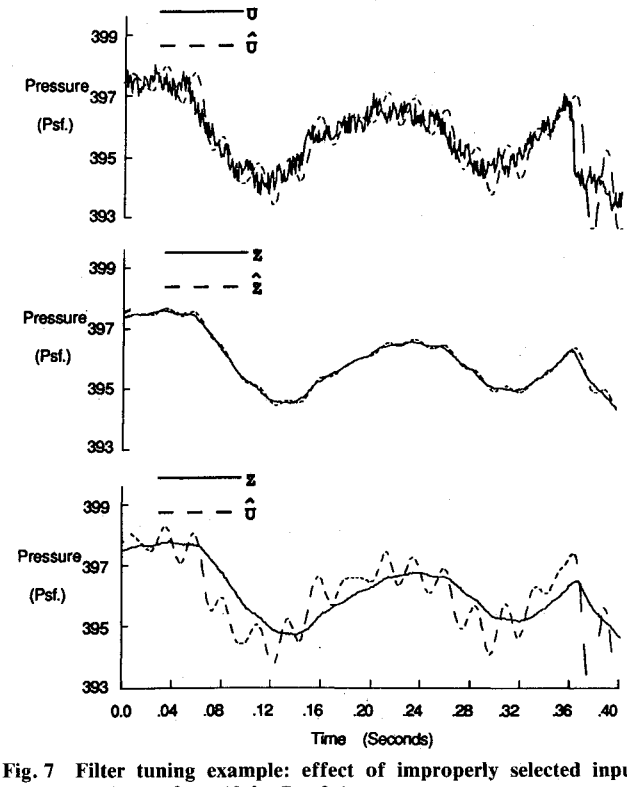

Fig. 7 Filter tuning example: effect of improperly selected input error covariance, $Q_u = 10.0$, $G = 0.1$.

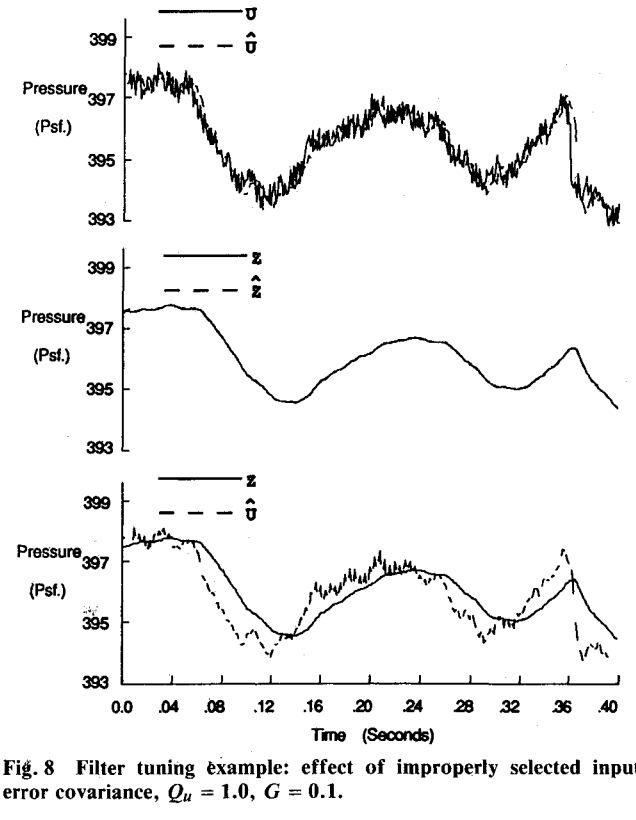

Fig. 8 Filter tuning example: effect of improperly selected input error covariance, $Q_u = 1.0$, $G = 0.1$.

input estimate. For the value of G chosen, the second term of Eq. (5c) (the measurement update) is large and overwhelms the first term (the residual update); the result of which is overamplification of the measurement noise. The estimator does not control noise in the measured pressure output.

Figure 7 demonstrates the effect that selected values of Q_U have on the estimation of U. In this figure the value of G is fixed at the actual value of 0.01 lbf/ft^2, whereas the value for Q_U is set at 10.0 lbf/ft^2. Recall that the actual value for Q_U is

1.0 lbf/ft^2. The resulting estimate exhibits extraneous harmonics caused by overamplification of midrange frequencies not present in the original input. The dynamic constraints of the second-order model have not been enforced strongly enough.

An example of the appropriate level of smoothing and compensation is presented in Fig. 8. Here the actual values for the measurement and input error covariances are used. In this case, the estimated input matches the actual input very well, and much of the superimposed noise has been removed.

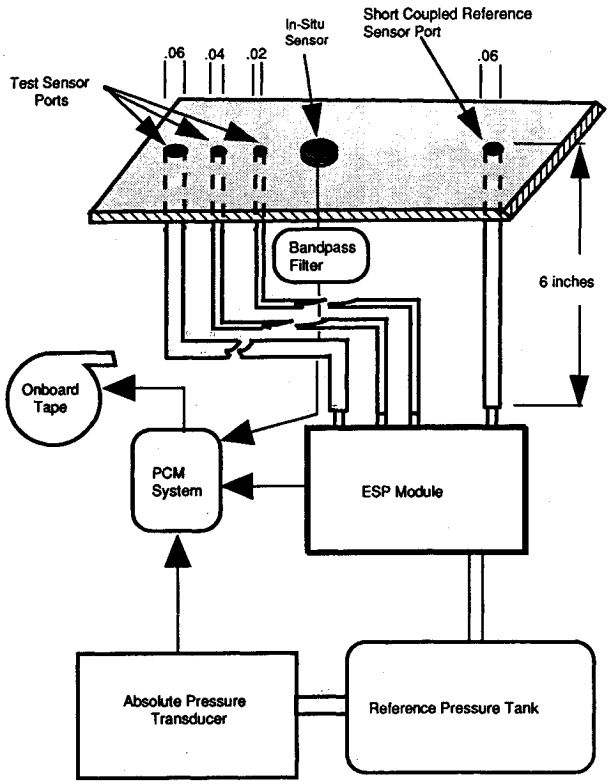

Fig. 9 Schematic of flight test experiment.

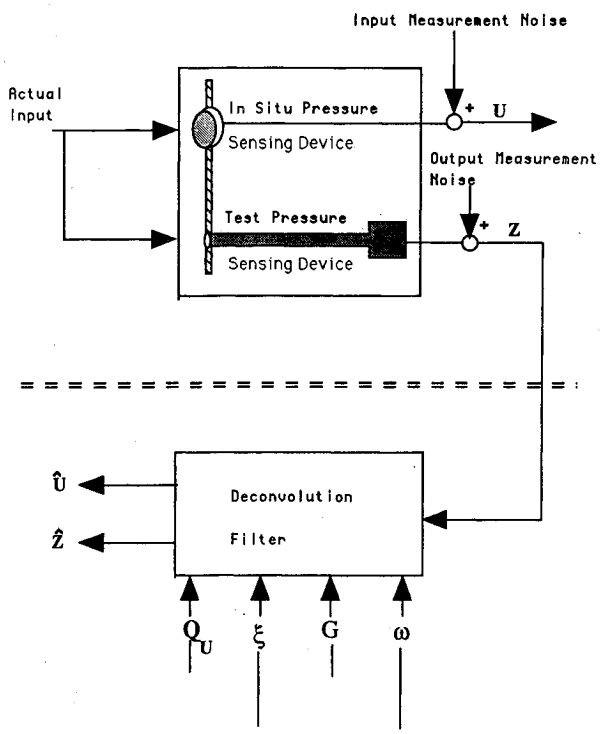

Fig. 10 Schematic of flight data deconvolution algorithm.

Application to Flight Data

The deconvolution algorithms are now applied to flight data resulting from the experiments described in Refs. 1-4 and 15. The flight test configuration mounted on the wing of a high-performance aircraft, Fig. 9, consisted of a set of static test orifices connected by pneumatic tubing to a single electronically scanned pressure module (ESP). The test matrix, whose ports had diameters of 0.02, 0.04, and 0.06 in., allowed pneumatic tubing sections to be easily interchangeable. Reference pressure data were provided by an in situ piezoelectric micro-

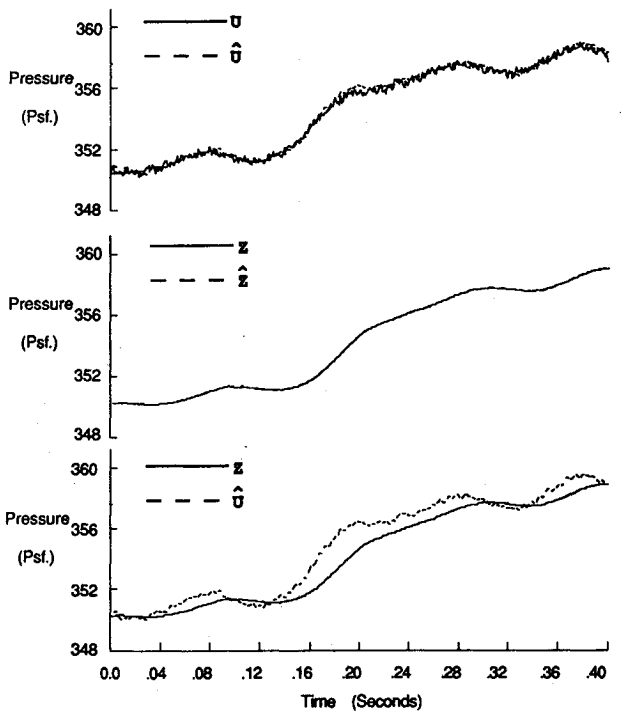

Fig. 11 Flight maneuver time history comparison I: output from the postflight deconvolution smoothing algorithm for an overdamped system.

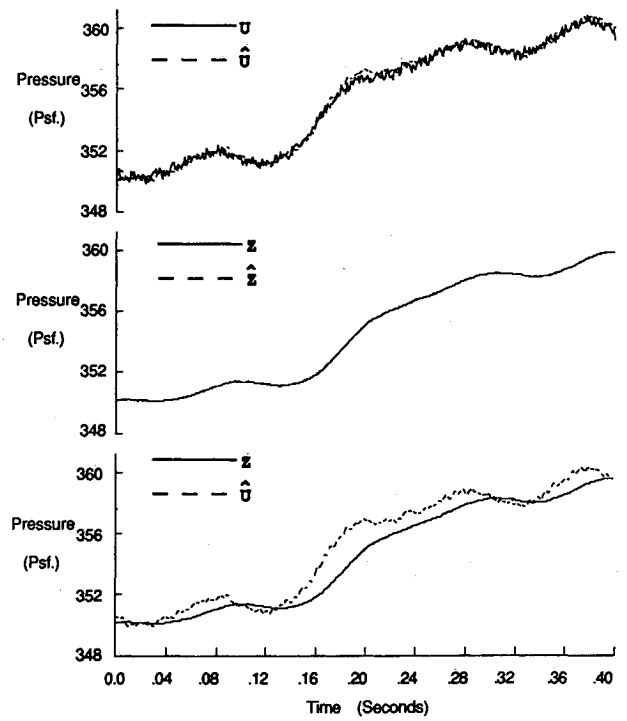

Fig. 12 Flight maneuver time history comparison I: output from the real-time deconvolution filtering algorithm for an overdamped system.

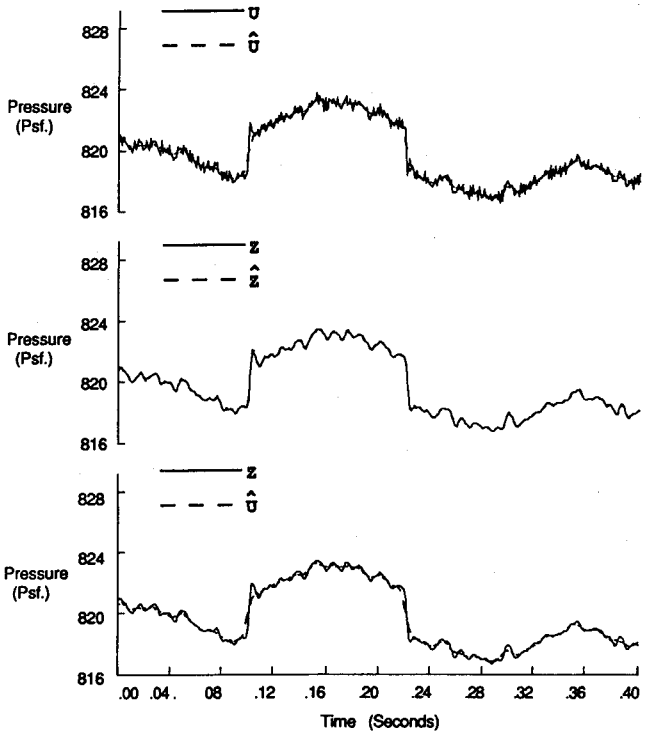

Fig. 13 Flight maneuver time history comparison II: output from the postflight deconvolution smoothing algorithm for underdamped sensor configuration.

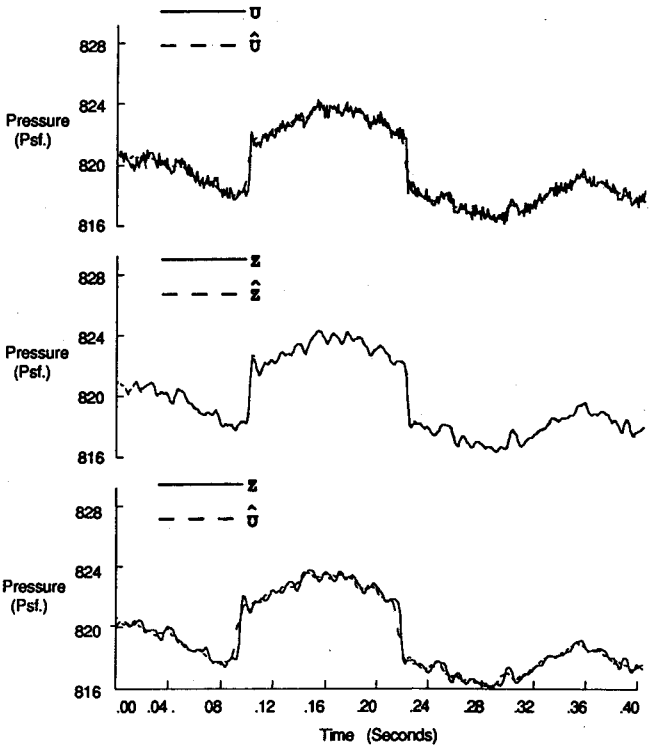

Fig. 14 Flight maneuver time history comparison II: output from real-time deconvolution filtering algorithm for underdamped sensor configuration.

phone transducer glued to the aircraft skin adjacent to the test matrix. The experimentally determined flat frequency response band of the reference transducer extended from 1.16 to 101.7 Hz. Direct-current (DC) components were added to the reference measurements using the output from a pressure port connected to the ESP module by a 6-in.-long, 0.06-in.-diam section of pneumatic tubing whose output was low-pass filtered using a second-order digital filter with a rolloff frequency at 1.16 Hz. The two filtered signals were merged using a complementary filter.[4]

Pressure data obtained from the test matrix measurements are compensated using both the postflight smoothing and real-time filtering algorithms, and are compared to the reference data. The flight data deconvolution process, similar to the simulation process described earlier, is depicted in Fig. 10. In this figure, the test pressure data Z are used to perform the deconvolution. The reference data U are assumed to represent the true input. The results of the deconvolution, $\hat{Z}$ and $\hat{U}$, are compared against the measured data values. All tuning of the filter covariances is performed off-line using prior knowledge of the measurement system accuracies.[2,3,15]

Deconvolution results for an overdamped flight maneuver obtained at 42,000-ft altitude with a sensor configuration having an 8-ft-long, 0.06-in.-diam pneumatic tubing and negligible transducer volume are presented in Fig. 11 for the smoothing algorithm and in Fig. 12 for the filtering algorithm. For this configuration and altitude, the damping ratio of the second-order model is 2.125, and the natural frequency is 26.75 Hz. As with the earlier simulation comparisons, three time history plots are shown. The lower graph compares the estimated input ($\hat{U}$) with the measured output (Z). The middle graph compares the measured (Z) and predicted ($\hat{Z}$) outputs. The upper graph compares the reference input data (U) to the estimated input ($\hat{U}$). The comparisons are excellent for both the postflight smoothing and real-time filtering algorithms. Note that the estimated input does not contain the high-frequency noise present in the reference data.

Deconvolution results for an underdamped flight maneuver obtained at 24,000-ft altitude with a sensor configuration having a 2-ft-long, 0.06-in.-diam pneumatic tubing and negligible transducer volume are presented in Fig. 13 for the smoothing algorithm and in Fig. 14 for the filtering algorithm. For this configuration and altitude, the equivalent damping ratio of the second-order system is 0.279; the natural frequency is 107.18 Hz. Both the smoothing and filtering algorithms work well. The smoothing algorithm removes nearly all of the resonant harmonic at approximately 100 Hz. The filtering algorithm removes a sizable portion of the resonance. Both algorithms account for phase lag very well.

Summary and Concluding Remarks

The emphasis of this paper was on the development of a general numerical technique by which unsteady pressure measurements might be obtained using conventional pressure sensing technology. A mathematical model, based on the unsteady equations of momentum and continuity, was reduced to a simple second-order state-variable model. Frequency response comparisons of the full- and second-order models were presented. Using a collection of standard results from minimum-variance estimation theory, the second-order model was incorporated into a deconvolution algorithm that estimated the system input based upon observations of the system output. Both postflight smoothing and real-time filtering algorithms were developed. Overamplification of measurement error is controlled by judicious selection of the elements of the algorithm state and measurement error covariance matrices. Performance characteristics were discussed. Filter tuning characteristics were illustrated using simulated data. Applications of the techniques to flight data were presented. Results presented verify that, given appropriate covariance magnitudes, the algorithms accurately reconstruct surface pressure values from remotely sensed pressure measurements.

The results of this research indicate considerable promise for the modeling and compensation techniques, as developed. These techniques provide a means by which the effects of pneumatic distortion in pressure sensing devices can be predicted and accounted for. Application of these techniques offers a reliable and cost effective means of measuring unsteady pressure data. These techniques will help to bridge the

gap until new pressure sensing technologies can be sufficiently matured.

References

[1]Whitmore, S. A., "Formulation of a General Technique for Predicting Pneumatic Attenuation Errors in Airborne Pressure Sensing Devices," NASA TM-100430, May 1988.

[2]Whitmore, S. A., Curry, R. A., Gilyard, G. B., and Lindsey, W. C., "The Effects of Pneumatic Tubing on Unsteady Pressure Measurements," NASA TM-4171, March 1990.

[3]Whitmore, S. A., "Formulation and Verification of a Technique for Compensation of Pneumatic Attenuation Errors in Airborne Pressure Sensing Devices," Ph.D. Dissertation, Univ. of California, Los Angeles, University Microfilms International, 1989.

[4]Whitmore, S. A., and Moes, T. A., "The Effect of Pressure Sensor Acoustics on a High Angle-of-Attack Flush Airdata Sensing System," AIAA Paper 91-0671, Jan. 1991.

[5]Lamb, J. P., "The Influence of Geometry Parameters Upon Lag Error in Airborne Pressure Measurement Systems," WADC TR 57-351, Wright-Patterson AFB, OH, July 1957.

[6]Iberall, A. S., "Attenuation of Oscillatory Pressures in Instrument Lines," National Bureau of Standards, RP 2115, Washington, DC, July 1950.

[7]Schuder, C. B., and Binder, R. C., "The Response of Pneumatic Transmission Lines to Step Inputs," *Journal of Basic Engineering*, Vol. 81, No. 6, 1959, pp. 578-584.

[8]Berg, H., and Tijdeman, H., "Theoretical and Experimental Results for the Dynamic Response of Pressure Measuring Systems," National Lab. for Research, Rept. F.238, Amsterdam, 1965.

[9]Schlicting, H. R., *Boundary Layer Theory,* 4th ed., McGraw-Hill, New York, 1979.

[10]Franklin, G. F., and Powell, J. D., *Digital Control of Dynamic Systems,* Addison-Wesley, Reading, MA, 1980.

[11]Mendel, J. M., *Optimal Seismic Deconvolution, An Estimation Based Approach,* Academic Press, New York, 1983.

[12]Chi, C. Y., and Mendel, J. M., "A Fast Approach to Identification Using Deconvolution," *Proceedings of the Conference on Decision and Control,* Inst. of Electrical and Electronics Engineers, Vol. 3, 1983, pp. 1347-1352.

[13]Chi, C. Y., "A Further Analysis of Minimum Variance Deconvolution Performance," *IEEE Transactions on Acoustics, Speech, and Signal Processing,* Vol. ASSP-35, No. 3, 1987, pp. 888, 889.

[14]Meditch, J. S., *Stochastic Optimal Linear Estimation and Control,* McGraw-Hill, New York, 1969.

[15]Curry, R. E., and Gilyard, G. B., "Flight Evaluation of a Pneumatic System for Unsteady Pressure Measurements Using Conventional Sensors," NASA TM-4131, Aug. 1989.